

The spring minimum in subseasonal 2-meter temperature forecast skill over North America

Melissa L. Breeden^{a,b}, John R. Albers^{a,b}, Amy H. Butler^c, and Matthew Newman^{a,b}

a. Cooperative Institute for Research in Environmental Sciences, University of Colorado
Boulder, Boulder, CO

b. NOAA Physical Sciences Laboratory, Boulder, CO

c. NOAA Chemical Sciences Laboratory, Boulder, CO

Corresponding author: Melissa L. Breeden, melissa.breeden@noaa.gov

ABSTRACT

On average, 2-meter temperature forecasts over North America for leads greater than about two weeks have generally low skill in operational dynamical models, largely because of the chaotic, unpredictable nature of daily weather. However, for a small subset of forecasts, more slowly evolving climate processes yield some predictable signal that may be anticipated in advance, occasioning so-called ‘forecasts of opportunity’. Prior research has demonstrated that for boreal winter, an empirical dynamical modelling technique called a linear inverse model (LIM), whose forecast skill is typically comparable to operational forecast models, can successfully identify forecasts of opportunity both for itself and for other dynamical models. In this study, we use a set of LIMs constructed from weekly-averaged tropical outgoing longwave radiation (OLR) and Northern Hemisphere streamfunction anomalies, obtained from the Japanese 55-year Reanalysis dataset, to examine how subseasonal North American 2-meter temperature potential predictability and forecasts of opportunity vary from boreal winter through summer. We show how LIM skill evolves during the three phases of the spring transition of the north Pacific jet - late winter, spring, and early summer - revealing clear differences in each phase and a distinct skill minimum in spring. We identify a subset of forecasts with markedly higher skill in all three phases, despite LIM temperature skill that is somewhat low on average. However, skill improvements are only statistically significant during winter and summer, again reflecting the spring subseasonal skill minimum. The spring skill minimum is consistent with theory and arises due to a minimum in the LIM’s forecast signal-to-noise ratio.

1. Introduction

Routinely producing skillful subseasonal (3-8 week lead) 2-meter temperature (2mT) and precipitation forecasts remains difficult for the current generation of dynamical subseasonal forecast models in all seasons (Pegion et al. 2019, de Andrade 2020). As a result, much attention has been given to identifying the smaller subset of subseasonal forecasts that *are* useful, by considering phenomena that impart memory, and therefore predictability, to the system – so-called forecasts of opportunity (Albers and Newman 2019; Mariotti et al. 2020). These more skillful forecasts reflect periods of high signal-to-noise ratio, or when a predictable ‘signal’ overwhelms unpredictable ‘noise’ in the system evolution. Predictable signals in the extratropics can arise through many processes including tropical-extratropical teleconnections (Winkler et al

2001), stratosphere-troposphere interactions (Baldwin et al. 2003; Butler et al. 2019a; Domeison et al. 2020; Albers and Newman 2021a), and long-lasting soil moisture anomalies (Koster et al. 2011). Which processes are most important for forecasts of opportunity is determined by forecast location, target variable, forecast lead-time, and time of year.

A key source of subseasonal predictability in the Pacific-North American region is tropical diabatic heating (e.g., Newman et al. 2003). For example, elevated North American temperature skill follows certain phases of the Madden-Julian Oscillation (MJO, Madden and Julian 1971, Johnson et al. 2014; Vigaud et al. 2018) and the El Niño – Southern Oscillation (ENSO; Johnson et al. 2014; Wang and Robertson 2018). However, skill provided by the MJO and ENSO is not constant at all times of the year, in part because the nature of tropical convection evolves over the course of the annual cycle. Convection related to ENSO tends to weaken during spring, particularly following its mature winter phase, while the extratropical influence of tropical heating via teleconnections varies due to the annual cycle of the Pacific jet and waveguide (Newman and Sardeshkhukh 1998). In addition to tropical heating, stratospheric variability can affect North American temperatures during winter and early spring before the final stratospheric warming, with some stratospheric states being associated with elevated subseasonal temperature forecast skill (Gerber et al. 2012; Butler et al. 2019b; Domeison et al. 2020).

Perhaps as a result of these seasonally-varying phenomena, spring is a particularly difficult forecast period. In a recent study, Albers et al. (2021b) found that the ability of the European Centre for Medium Range Weather Forecasting Integrated Forecast System (IFS) to predict variations in the North Pacific jet decreases markedly between early and late spring. This decrease in subseasonal skill could be related to the strong invigoration of the north Pacific storm track that occurs during this time of year (Breedon et al. 2021), representing an increase in unpredictable synoptic variability. Another possibility is that models have difficulty modeling the smaller spatial scales of tropical heating that tend to increasingly dominate tropical variability as spring progresses into summer (Newman and Sardeshkhukh 1998). It is perhaps not surprising then, that spring temperature predictability has not been extensively studied compared to winter and summer. In this study, we hypothesize that seasonal changes in both the jet and tropical heating correspond to a reduction in subseasonal temperature predictability during spring.

Prior analysis has demonstrated the utility of an empirical-dynamical linear inverse model (LIM; Penland and Sardeshmukh 1995; Sardeshmukh et al. 2000) to generate subseasonal forecasts and objectively identify forecasts of opportunity. During winter, a LIM can produce 500-hPa geopotential height and mean sea level pressure forecasts with skill comparable to the National Centers for Environmental Prediction Climate Forecast System version 2 (CFSv2) and IFS for lead times of 3-6 weeks, while also identifying periods of elevated skill in its own forecasts and those of the CFSv2 and IFS (Albers and Newman 2019). A similar LIM produced subseasonal North Atlantic Oscillation (NAO) index forecasts with skill comparable to the IFS. In the latter LIM, NAO forecasts of opportunity were found to be due to SST-related heating anomalies and downward propagating stratospheric circulation anomalies (Albers and Newman 2021a). LIM forecasts during spring, however, have not been investigated in the present literature, nor has 2mT been selected as a target variable.

In this study, we employ a recently-introduced method for tracking the winter-to-summer evolution of the north Pacific jet, which we use to define the spring state of the jet on a flow-dependent, rather than calendar day, basis (Breedon et al. 2021). This approach ensures that the substantial year-to-year variability in the seasonal cycle of the north Pacific jet is accounted for, and anomalies developing in similar mean states are correctly grouped together. Three LIMs, similar to those used in Winkler et al. 2001 and Newman et al. 2003, are subsequently developed to produce late winter, spring and early summer forecasts of North American 2mT. An optimal growth approach to identifying forecasts of opportunity is employed, which successfully identifies periods of elevated circulation and 2mT skill. Finally, we compare observed skill to that expected from theory, and compare the evolution of predictable signal and unpredictable noise during the three jet phases to better understand the observed skill evolution.

2. Data and Methods

This study uses gridded reanalysis data to construct separate LIMs for the winter, spring and summer phases of the spring transition.

a. Data

Daily mean 200-hPa zonal wind, 200-hPa (Ψ_{200}) and 850-hPa (Ψ_{850}) streamfunction, 2-meter temperature (2mT), and outgoing longwave radiation (OLR) were accessed from the Japanese Meteorological Agency 55-year Reanalysis dataset (JRA-55; Kobayashi et al. 2015) for

the years 1959-2018 and months of January - July. All variables are regridded to $2.5 \times 2.5^\circ$ horizontal resolution. For tracking the spring transition of the north Pacific jet (described in Section 2b), we use 200-hPa zonal wind values for January – July, with only the 60-year January – July mean removed so that the seasonal cycle is retained, following the method of Breeden et al. (2021). Conversely, anomalies used in the LIM (Section 2c) were calculated by removing the 60-year daily climatology, and then applying a 7-day running mean to isolate weekly variability and minimize high-frequency, synoptic variations. Such averaging is consistent with the assumptions made by the modeling framework described below (Newman et al. 2003; Albers and Newman 2019).

b. Defining the spring transition

Following the approach in Breeden et al. (2021), we use the leading empirical orthogonal function (EOF1) and corresponding principal component (PC1) of 200-hPa zonal wind over the north Pacific domain (Fig. 1) to track the seasonality of the north Pacific jet. PC1 is positive during late winter and early spring, decreases throughout the spring transition, and becomes negative sometime in May or June. The substantial spread in PC1 early in the spring transition reflects the high variability in the jet and storm track at this time of year, and the limitation of using a single calendar date to define ‘spring’. Therefore, we instead use each year’s transition date when PC1 first falls below $+0.6\sigma$ to define the start of the spring phase. Similarly, when PC1 first falls below -0.6σ is used to define the beginning of the summer phase. The $\pm 0.6\sigma$ threshold was chosen to have a roughly even number of samples in the three phases ($N = 4986$ days in winter, 4055 days in spring and 4103 days in summer).

c. Linear Inverse Model

The LIM is based on the assumption that the dynamical evolution of the variables in the state vector \mathbf{x} (Eqn 1) can be reasonably approximated as a linear system forced by stochastic white noise (Eqn 2):

$$\mathbf{x} = \{\text{OLR}, \Psi_{200}, \Psi_{850}, 2\text{mT}\} \quad \{1\}$$

$$\frac{d\mathbf{x}}{dt} = \mathbf{L}\mathbf{x} + \mathbf{F}_s \quad \{2\} \quad .$$

Eqn 2 approximates the evolution of \mathbf{x} by assuming that a timescale separation exists between the predictable, slowly-evolving dynamics represented by \mathbf{L} and the fast, rapidly decorrelating and therefore unpredictable variations represented by \mathbf{F}_s . Here, as in previous studies (Winkler et al. 2001; Newman et al. 2003; Albers and Newman 2019; Henderson et al. 2020; Breeden et al. 2020), slowly-evolving refers to weekly-varying anomalies (consistent with the 7-day running mean applied to the anomalies in \mathbf{x}), and fast refers to shorter synoptic and mesoscale variations. \mathbf{L} can be determined from the time-averaged $\mathbb{C}\mathbf{0}$ and lagged covariance $\mathbb{C}\tau_o$ statistics of the state vector (Eqn 3):

$$\mathbf{L} = \log m(\mathbb{C}\tau_o * \text{inv}(\mathbb{C}\mathbf{0}))/\tau_o \quad \{3\}$$

To reduce dimensionality, \mathbf{x} is constructed from the principal components (PCs) resulting from empirical orthogonal function (EOF) analysis of each variable in the state vector, where enough PCs are retained to capture a majority of variance of each variable, while retaining a stable model (Table S1). A range of retained PCs was tested, and results are not sensitive to the exact number of PCs retained in \mathbf{x} (not shown). Here a training lag τ_o of 5 days is used, consistent with prior studies (Winkler et al. 2001; Breeden et al. 2020). Note that the matrix \mathbf{L} , often referred to as the ‘dynamic operator’, acts linearly on \mathbf{x} but can include both linear relationships and linear approximations to nonlinearities, that may be included in $\mathbb{C}\mathbf{0}$ and $\mathbb{C}\tau_o$. This is in contrast to, for instance, a model based upon linearized equations of motion.

1) LIM Hindcasts

Given initial conditions $\mathbf{x}(0)$, an infinite-member ensemble forecast for any lead time, τ , can be generated using \mathbf{L} by solving the homogeneous component of Eqn 2:

$$\mathbf{x}(\tau) = \mathbf{x}(0) \exp(\mathbf{L}\tau) = \mathbf{x}(0)\mathbf{G}(\tau) \quad \{4\}$$

Cross-validated hindcasts are created by removing 10% of the data, recomputing \mathbf{L} and creating forecasts using the portion of removed data as initial conditions (ICs). To evaluate the LIM hindcast skill, hindcasts are verified against the un-truncated, observed (i.e., reanalysis) anomalies using the anomaly correlation coefficient (ACC) at each grid point (e.g., Newman et al. 2003).

Theoretical expected forecast skill is computed, and compared to actual forecast skill, for the three phases of the spring transition using the anomaly correlation version of the LIM signal-to-noise ratio S at each gridpoint, ii (Sardeshmukh et al. 2000; Newman et al. 2003):

$$S^2(\tau, i) = \frac{F(\tau)_{ii}}{E(\tau)_{ii}}, \quad \{5\}$$

$$\mathbf{F}(\tau) = \langle \mathbf{x}(t + \tau) \mathbf{x}(t + \tau)' \rangle \quad \{6\}$$

$$\mathbf{E}(\tau) = \mathbf{C}\mathbf{0} - \mathbf{G}(\tau)\mathbf{C}\mathbf{0}\mathbf{G}(\tau)' \quad \{7\},$$

where $\mathbf{F}(\tau)$ is the forecast signal covariance matrix determined at a given lead time, indicating the strength of the predictable signal in the forecasts. $\mathbf{E}(\tau)$ is the forecast error covariance matrix and represents lead-dependent, unpredictable ‘noise’. S^2 is, in turn, used to calculate expected skill of a perfect infinite member ensemble forecast:

$$\rho_{\infty}(\tau) = \frac{S^2(\tau)}{\{[S^2(\tau)+1]S^2(\tau)\}^{.5}} \quad \{8\}.$$

Both $\rho_{\infty}(\tau)$ and the components of S^2 , that is, the signal and the noise, will be considered during the three jet phases and used to explain the observed and theoretical evolution of subseasonal 2mT skill.

2) Forecasts of Opportunity

Our approach to identifying forecasts of opportunity will focus on the signal component of signal-to-noise by anticipating periods of rapid, potentially predictable 2mT growth. The LIM is based on the concept that subseasonal anomaly growth can be modeled through the constructive interference of evolving nonorthogonal modes in the system that all have distinct spatial and temporal characteristics (Farrell 1988; Lacarra and Talagrand 1988; Farrell and Ioannou 1996). If the eigenmodes of \mathbf{L} are nonorthogonal, then transient anomaly growth may occur via the constructive interference of the eigenmodes over a finite period of time (because $\{2\}$ is asymptotically stable, the eigenvalues of \mathbf{L} are all negative and the individual eigenmodes all decay in finite time). Physically, the nonorthogonality of \mathbf{L} can arise from the presence of

asymmetric interactions in the system and patterns of variability that involve multiple physical processes evolving on different timescales (e.g., the NAO, Albers and Newman 2021a). Particularly relevant here are asymmetries introduced by shear and zonal asymmetry in the mean state (Farrell 1982; Boyd 1983), as observed in the North Pacific jet exit region (Mak and Cai 1989; Breeden and Martin 2018). The most rapidly growing patterns that amplify via transient growth can be determined using the eigendecomposition of system growth (Eqn 9; Penland and Sardeshmukh 1995, Newman et al. 2003). System growth $\mu(\tau)$ can be constrained to occur under a particular initial or final state, which can be set using the initial and final ‘norm’ kernels \mathbf{D} and \mathbf{N} , respectively:

$$\mu(\tau) = \frac{x(\tau)^T \mathbf{N} x(\tau)}{x(0)^T \mathbf{D} x(0)} = \frac{x(0)^T \mathbf{G}(\tau)^T \mathbf{N} \mathbf{G}(\tau) x(0)}{x(0)^T \mathbf{D} x(0)} \quad \{9\}$$

$$\mathbf{G}(\tau)^T \mathbf{N} \mathbf{G}(\tau) = \mu(\tau) \mathbf{v}(\tau) \quad \{10\}$$

The corresponding eigenvalues $\mu(\tau)$ determined from Eqn 10 represent the system growth rate associated with the evolution of the corresponding initial patterns contained in the eigenvectors $\mathbf{v}(\tau)$. The eigenmodes can be sorted from highest to lowest growth rate using the eigenvalues, and those with the strongest growth might be expected to be the most predictable. Growth is maximized for a prescribed period of τ days and without any constraint on the initial pattern, for which \mathbf{D} is set to the identity matrix, as done in past studies (e.g., Sardeshmukh et al. 1997; Newman et al. 2003). Commonly used norms include the L2 or ‘energy’ norm, in which \mathbf{N} is also set to the identity matrix. For this study, our final norm \mathbf{N} maximizes North American 2mT anomaly growth, which is specified by beginning with the identity matrix and setting the diagonals corresponding to the OLR, Ψ_{200} , Ψ_{850} PCs to zero, so that only 2mT amplitude is constrained to amplify. The resultant ‘optimal patterns’ (OPs) we describe in Section 3 are interpreted as the first and second patterns most conducive to 2mT growth, and will be referred to as OP1 and OP2, respectively. For each phase, we will examine the OP1 and OP2 maximizing 2mT growth over a 14-day period, as this is near peak amplification (not shown) but approaches subseasonal timescales (e.g., Breeden et al. 2020).

We identify forecasts of opportunity using the *optimal initial conditions*, determined from the eigenvectors of Eqn 10, that maximize 2mT growth of either OP1 or OP2. Specifically, we assume that forecasts initialized when the initial atmospheric state strongly resembles one of the

optimal initial conditions associated with either OP1 and OP2 will be followed by periods of elevated forecast skill. The hypothesized correspondence between strong projections onto the optimal initial conditions, and higher ACC, will be tested for the three phases of the spring transition using OP1 and OP2 for each phase, and the corresponding optimal initial conditions OP1-IC and OP2-IC. To identify forecasts of opportunity, we use the OP-ICs corresponding to a τ at the midpoint of the forecast lead time, for example, for week 3-4 forecasts (days 15-28), we determine OP-IC using a lead time $\tau = 21$ days. However, the structure of the ICs for the range of lead times considered (7-35 days) does not differ substantially (not shown), meaning that at this range of lead times, growth is arising from the same optimal pattern and its evolution. The 20% of dates with the strongest projection – positive or negative – onto a given OP-IC is selected as forecasts of opportunity, corresponding to 997 dates in winter, 811 in spring, and 820 in summer. The statistical significance of skill changes for each subset of forecasts is determined via bootstrapping, where the two groups of forecasts are resampled at the smaller sample size of the two groups, after it is reduced by five to account for autocorrelation in the 2mT field, which reduces the number of truly independent samples. Five is chosen because for 2mT, five days is the lag at which autocorrelation drops below 0.5 over North America. ACC is then recomputed for that sub-sample, and the process repeated 5000 times to establish confidence intervals for ACC at each gridpoint.

3. Results

The three phases of the spring transition of the north Pacific jet show its seasonal evolution from the strong, wintertime jet to a weaker, split jet during spring, and finally, a very weak summer jet structure (Fig. 1). The onset of the spring phase coincides with an invigoration and northward shift of the north Pacific storm track, which is followed by relatively quiescent storm track conditions during summer (Breedon et al. 2021). The winter-to-spring transition is highly variable but typically occurs in late March or April, while the spring-to-summer transition is less variable and generally occurs in late May (Fig. 1d). In Section 3a, we compare the OP1 and OP2 patterns during each jet phase, revealing the patterns are all notably different. Section 3b examines the corresponding evolution of LIM 2mT hindcast skill, and evaluates the success in using OP1-IC and OP2-IC to identify forecasts of opportunity. To better understand the observed forecast skill evolution, Section 3c considers theoretical expected skill and the seasonal evolution of the signal (Eqn 6) and the noise (Eqn 7).

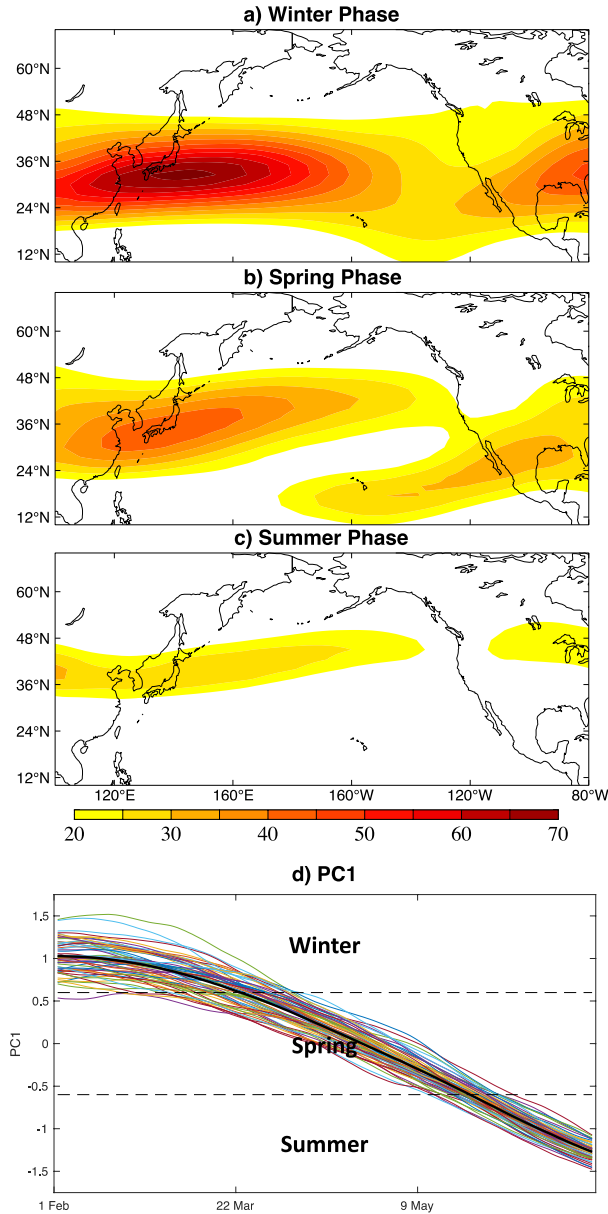


Fig. 1: Panel a) shows composite 200-hPa zonal wind (units m s^{-1}) based on periods when a) $\text{pc1} > 0.6\sigma$, the ‘winter phase’, b) $\pm 0.6\sigma$, the ‘spring phase’, and c) $< -0.6\sigma$, the ‘summer phase’. The thin lines in panel d) show PC1 for each year in the 60-year JRA55 record, starting on 1 February through 27 June, and the thick black line is the 60-year mean.

a. Optimal 2-meter temperature structures

Under the constraint to maximize North American 2mT anomaly growth (Eqn 10), each phase of the jet is associated with different heating and circulation structures (Figs. 2-4). Note that because of the linearity of the LIM, equal and opposite patterns (e.g., warm anomalies instead of cold anomalies in Fig. 2b) correspond to equal and opposite signs of all variables.

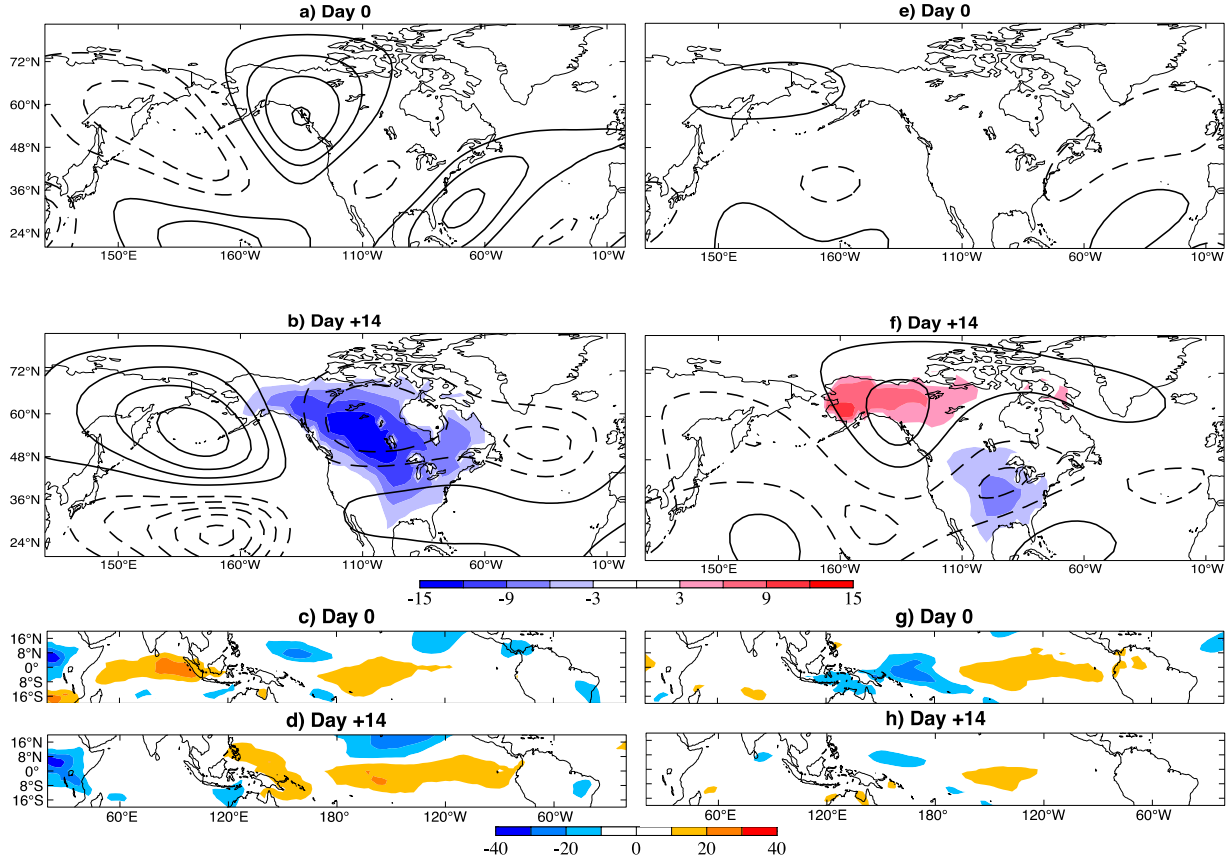


Fig. 2: First (a-d) and second (e-h) optimal patterns (OP1, OP2) maximizing North American 2-meter temperature growth, over a 14-day period, during the winter jet phase. The color shading in a), b), e), f) is anomalous 2mT in units degrees Celsius, and the black contours are 200-hPa streamfunction anomalies (positive in solid, negative in dashed). The contour interval for streamfunction is $\pm 5 \times 10^6 \text{ kg m}^2 \text{ s}^{-1}$ contoured at intervals of 5×10^6 . The color shading in c), d), g), h) is anomalous OLR in units W m^{-2} .

During the winter phase (Fig. 2), OP1-IC involves an upper-level ridge in the east Pacific and negligible 2mT anomalies; 14 days later, widespread cold anomalies develop in conjunction with a blocking anticyclone upstream over the central Pacific. Meanwhile, positive OLR anomalies (representing suppressed convection) are located over the eastern Indian ocean and central Pacific at Day 0, with the former propagating eastward with time and the latter remaining stationary (Fig. S1a-c). Much of the evolution resembles that of North Pacific blocking, whose subseasonal evolution can be well-produced by a LIM (Breedon et al. 2020). OP2 is associated with a couplet of temperature anomalies with centers over Alaska and the central U.S (Fig. 2f) and a dipole of stationary OLR anomalies in the Pacific basin that decay with time (Fig. 2g-h; Fig. S2a-c).

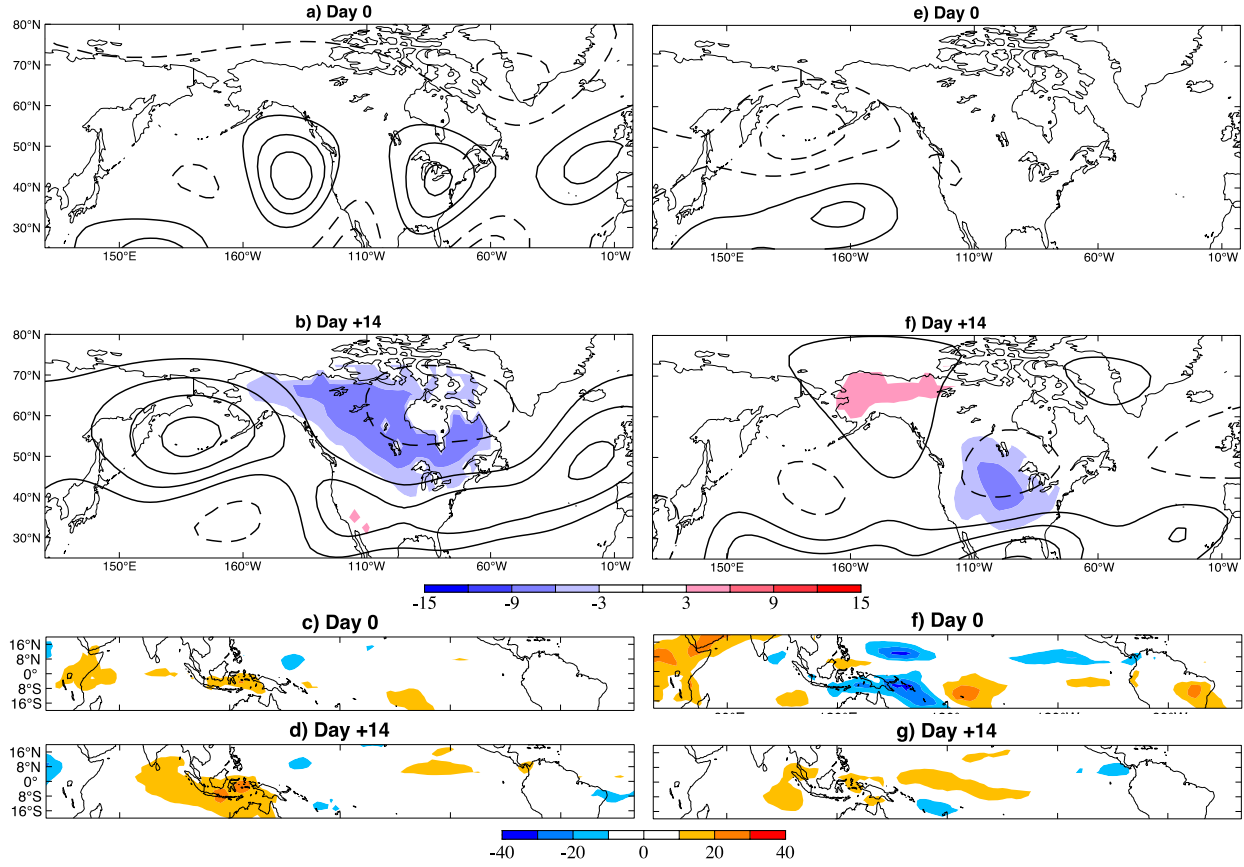


Fig. 3: As in Fig. 2 but for the first and second spring optimal growth structures.

During the spring jet phase (Fig. 3), the 2mT and Ψ_{200} final evolved anomalies resemble the OP1 structures in winter (cf., Figs. 2b to 3b and 2f to 3f), but with overall weaker and northward-shifted temperature anomalies – coincident with the northward shift of the jet – and the development of weak warm anomalies over the southwestern United States. Interestingly, the optimal initial conditions differ substantially. For example, the winter phase OP1 optimal initial condition resembles the Pacific-North American pattern, while the spring phase OP1 optimal initial condition is weaker, more zonal, and located further equatorward. The OLR evolution between the winter and spring phases differs as well, most notably a lack of stationary OLR anomalies in the central Pacific during spring (Fig. 3c-d; Fig. S1d-f). This lack of persistent, ENSO-like convection is consistent with the frequently observed decay of ENSO events during spring, meaning the associated teleconnection likely weakens at this time of year. While a propagating OLR feature is observed in the Indian ocean during spring, it is located farther to the west than what develops in winter, further reflecting changes in the optimal heating conditions

for 2mT growth from winter to spring. OP2 during spring also resembles OP2 in winter, although again with differences in the amplitude and precise location of the temperature and Ψ_{200} anomalies.

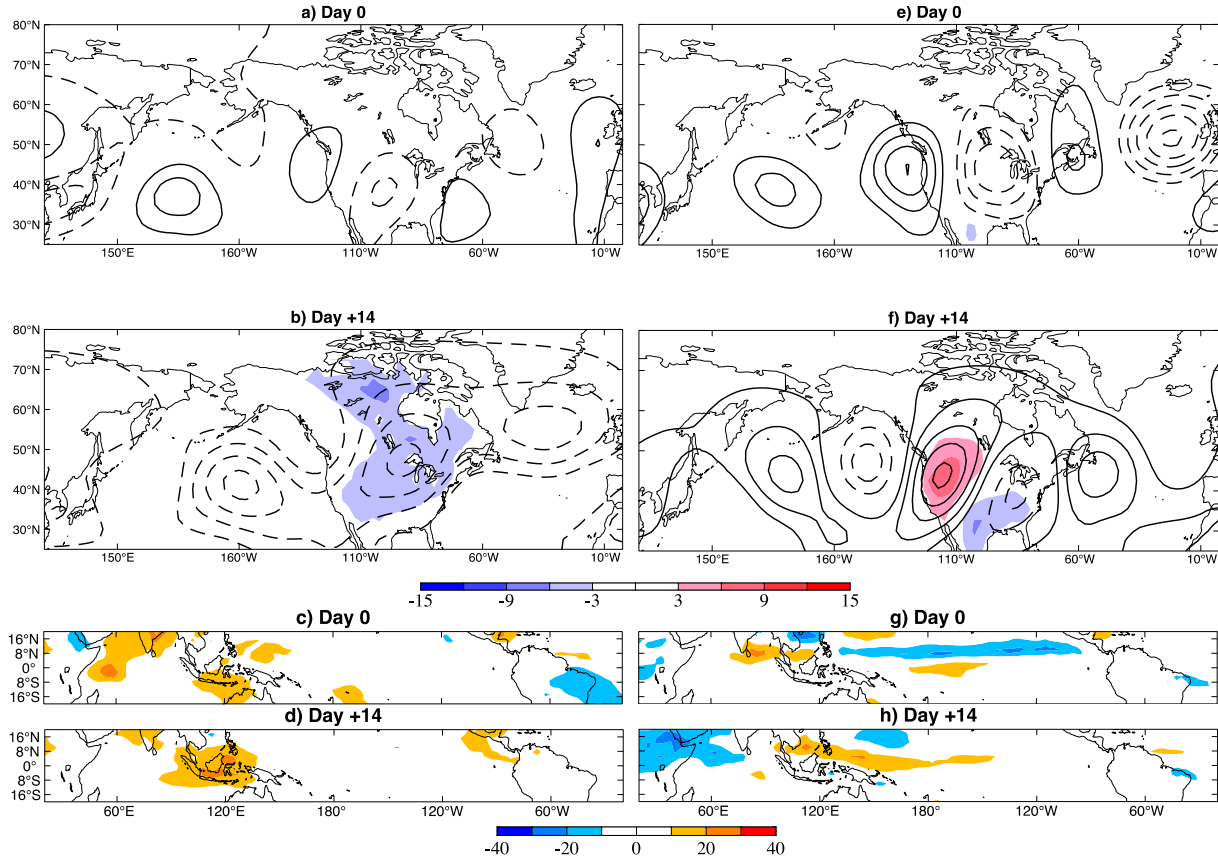


Fig. 4: As in Fig. 2 but for the first and second summer optimal growth structures.

The OPs that evolve in summer differ substantially from those in winter and spring (Fig. 4). In summer, OP1 involves cyclonic Ψ_{200} anomalies over the central Pacific, North America and North Atlantic that develop along with cold temperature anomalies over central North America (Fig. 4a-b). Positive OLR anomalies form over the Maritime Continent and are mainly stationary, persisting from initialization to past 40 days (Fig. 4c-b; Fig S1 g-i). While there is some consistency between cold temperatures and suppressed convection in the Indian Ocean and Maritime continent between all three phases' OP1 patterns, the circulation response at 200-hPa differs substantially in summer, suggesting the nature of the summer teleconnection differs from winter and spring, as found in Newman et al. (2003) for winter and summer. Finally, OP2 in summer involves development of a small-scale, zonally-oriented wave train over the central Pacific and North America, while tropical OLR involves a persistent negative anomaly centered

at 25°E (Fig. 4e-h). This circulation pattern strongly resembles the wave train that has recently been linked to surface moisture deficits over the Ohio river valley region during spring (Jong et al. 2022), which are influenced by vertical motions driven by the wave train. Overall, from winter to summer, the OP-ICs progressively shrink in zonal wavelength, consistent with the monthly evolution of North American height sensitivities to remote tropical heating found by Newman and Sardeshmukh (1998).

b. 2-meter temperature Skill Evolution

Subseasonal temperature skill evolves during the three phases of the spring transition, but in all phases, periods of elevated forecast skill are identifiable ahead of time using OP1-IC and OP2-IC. On average, week 3-6 2-meter temperature skill from LIM forecasts is low (Figs. 5-6), but similar to dynamical forecast models (Pegion et al. 2019; Wang and Robertson 2018). We find that temperature skill is greatest during winter, reaching a spatial minimum in spring before increasing again in summer (Fig 5a-c).

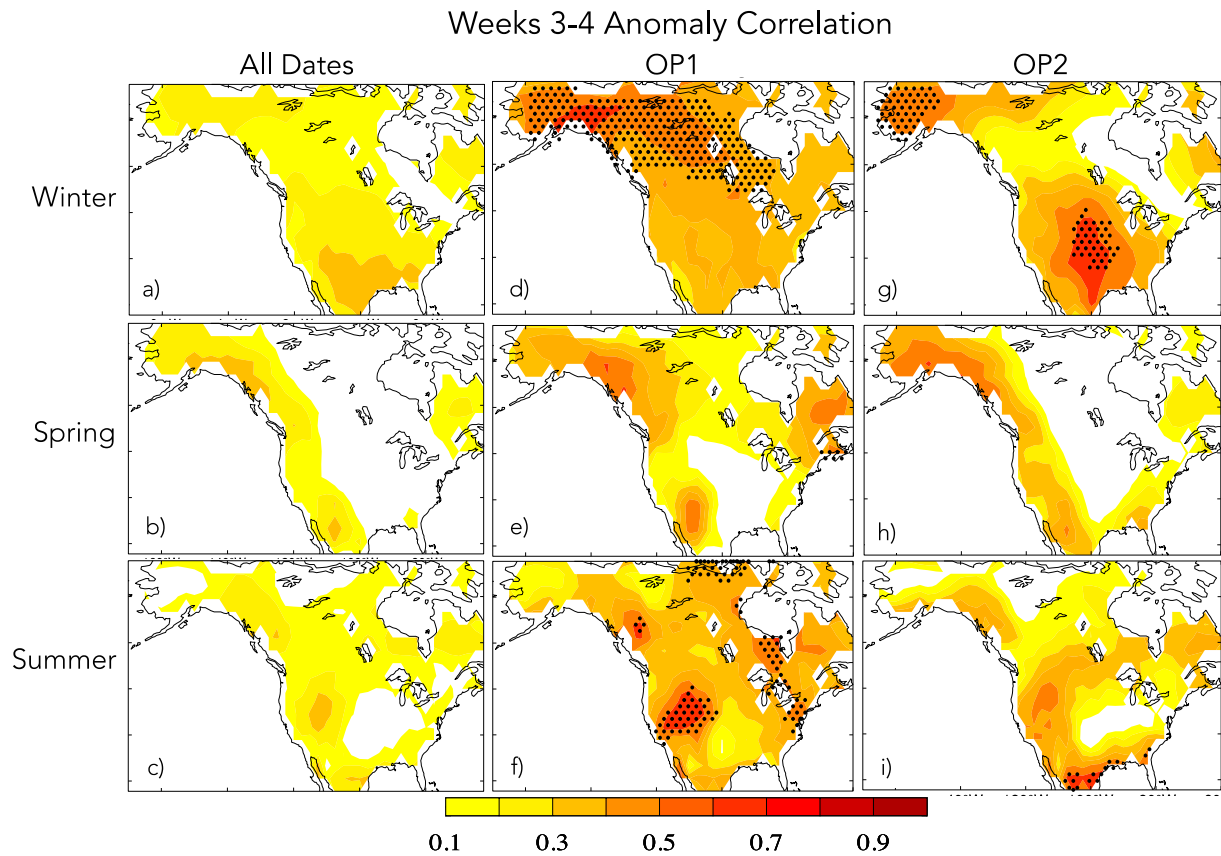


Fig. 5: Anomaly correlation coefficient (ACC) for weeks 3-4 temperature forecasts. The left column shows ACC using all forecasts during a) winter, b) spring and c) summer. The middle column shows ACC for the 20% of forecasts with the strongest projection onto the optimal initial

conditions associated with OP1, and the right column shows ACC for the 20% of forecasts with the strongest projection onto the optimal initial conditions associated with OP2. Stippling on panels d) – i) indicates where skill changes are significant at the 95% confidence level.

Nonetheless, even during the spring minimum, some skill is present in western North America from Alaska to Mexico (Fig. 5b). More encouraging, however, is that in all three phases, skill increases markedly for the forecasts initialized during the 20% of dates with the strongest projection – positive or negative – onto OP1-IC (Fig 5d-f). Skill is significantly different from the skill of the remaining 80% of forecasts during winter and summer, but not spring. Similarly, skill increases following strong projections onto OP2-IC, albeit over a smaller area during spring compared to winter and summer (Fig. 5g-i). The regions of highest skill generally coincide with the areas of strong OP growth, further supporting the idea that predictable anomaly growth is associated with the enhanced skill (c.f., Fig. 2b, 5d; Fig 4b, Fig. 5g). However, in spring, even for OP1 the spatial extent of ACC is confined to western North America, suggesting something is preventing strong optimal 2mT growth at this time.

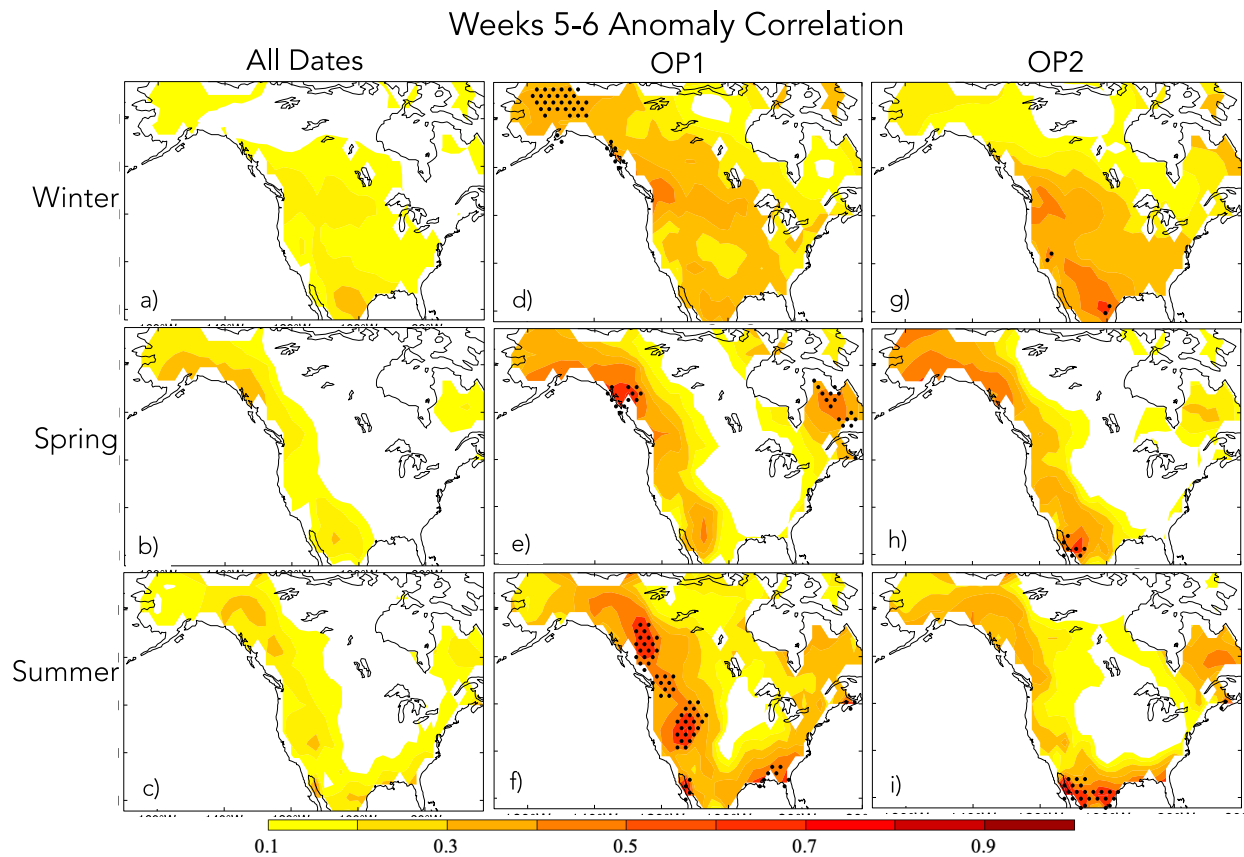


Fig. 6: As in Fig. 5 but for weeks 5-6 forecasts.

For weeks 5-6 forecasts, skill is lower than weeks 3-4 (Fig. 6a-c), yet there are still regions with reasonably high skill (correlations between 0.4-0.6), particularly during summer for OP1 (Fig. 6f). Furthermore, spring skill is similar at weeks 5-6 and is statistically significantly different for OP1 and 2 in some areas, though these are still spatially confined to coastal areas where it is possible high-frequency fluctuations are weaker due to the nearby water, enhancing the impact of the predictable signal (Fig. 6e, h).

It thus appears that the predictable temperature patterns, and their optimal initial conditions, are indeed associated with an increase in the predictable ‘signal’ in subseasonal forecasts, leading to an increase in skill. There are notable differences in when and where skill maximizes (Figs 5-6) during each of the three jet phases, but western North America is broadly the region with the most consistent skill. The spring phase displays the lowest overall skill and the weakest skill increase associated with forecasts of opportunity using OP1 and OP2, consistent with prior studies that have found a reduction in subseasonal forecast skill over the Pacific-North American region in spring (Wang and Robertson 2018; Albers et al. 2021).

c. Expected Skill

Does the spring skill minimum reflect a change in predictable signal, unpredictable noise, or some combination of both? To address this question, we consider the theoretical expected skill, ρ_{∞} (Eqn 8), for the three jet phases using the 21-day forecast signal-to-noise ratio (Fig. 7). The ρ_{∞} evolution and spatial characteristics are quite similar to the observed ACC (Fig. 5a-c), though ρ_{∞} is higher in all phases, as actual skill may be lower due to model imperfections or initial condition errors (Newman et al. 2003). During the winter phase, both the signal and noise components have the greatest amplitude, with the signal extending farther southwestward and accounting for the skill maximum located at more southern latitudes (Fig. 7a,d,g). In spring, there is a minimum in ρ_{∞} over most of North America, except in the far northern regions including Alaska, where the observed spring skill is also highest (c.f., Fig. 7b, Fig. 5b). The signal component reaches its minimum amplitude at this time, while noise has diminished as well but to a lesser extent, overall reducing ρ_{∞} in spring compared to winter and summer.

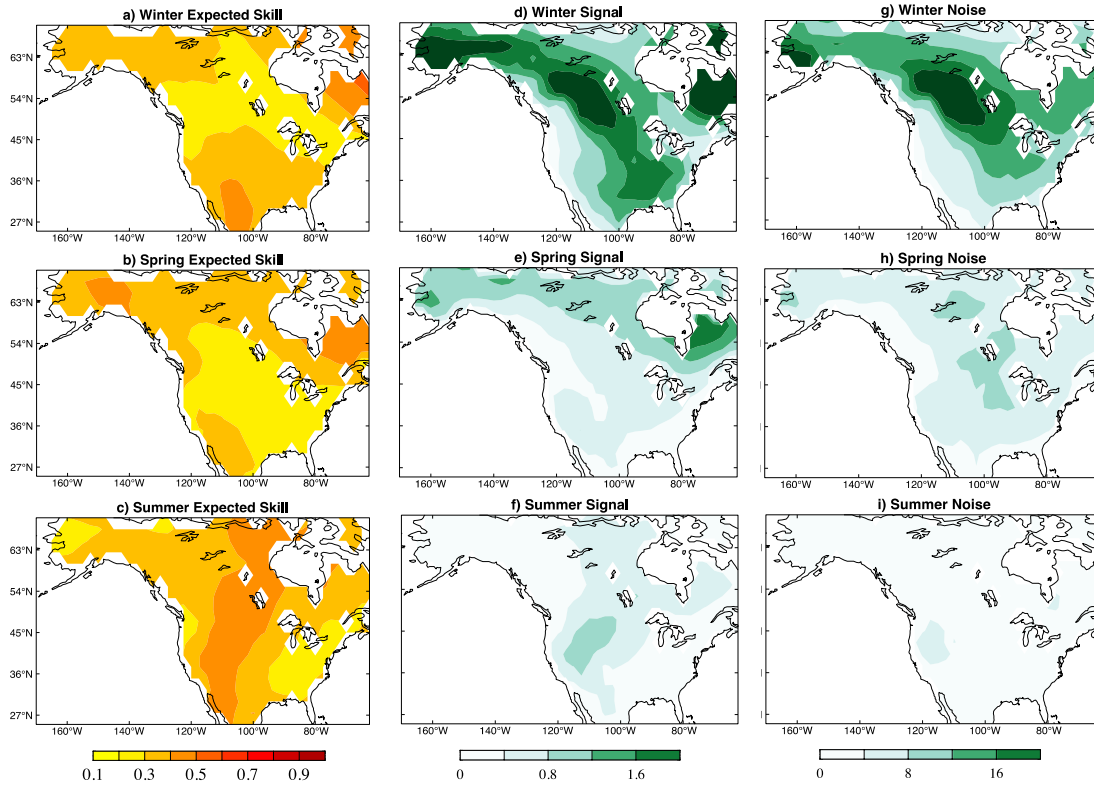


Fig. 7: Panels a) – c) show expected skill (units ACC; Eqn 8) calculated for the three phases of the spring transition. Panels d) – f) show the forecast signal covariance component of expected skill (\mathbf{F} , Eqn 6) and panels g) – i) show the error covariance component of expected skill (\mathbf{E} , Eqn 7). Units for \mathbf{F} and \mathbf{E} are K^2 .

The relatively elevated noise in spring in the interior of the continent could account for the lack of ACC increase during forecasts of opportunity associated with OP1 and OP2 (Fig 5e,h, 6e,h). In the summer phase, signal increases in the central US compared to spring, while noise continues to weaken, driving up the signal-to-noise ratio (S^2) and ρ_∞ to peak values in the interior continent (Fig. 7c). As such, it appears the observed skill minimum in spring is consistent with theoretical expected skill and the evolution of predictable signal and unpredictable noise components of the forecasts. It is notable that the signal and noise reach their minimum amplitudes at different times of the year, though the underlying mechanism for their different temporal evolutions is not well understood at present.

4. Discussion and Conclusions

In this study, we document predictable North American 2mT patterns, their evolution during three phases of the seasonal cycle, and test the hypothesis that they can be used to

anticipate subseasonal forecasts of opportunity. We find that notably different patterns of upper-level circulation and tropical OLR maximize 2mT growth during the winter, spring and summer phases of the north Pacific jet. Some patterns are familiar, or contain familiar elements, such as OP1 in winter and the PNA pattern. The associated tropical heating evolution maximizing 2mT growth differs in each phase as well, but overall reveals a role for stationary and propagating heating anomalies in the Indian Ocean, Maritime Continent and central Pacific. As such, ENSO, the MJO, and perhaps the Indian summer monsoon, may all be influencing subseasonal 2mT amplification, though further analysis is needed to confirm these potential links.

In all three phases, we are able to leverage knowledge of these predictable patterns to anticipate, at the time of forecast initialization, forecasts of opportunity for 2mT, with the most success in winter and summer. Skill reaches a minimum in spring, and over much of North America, skill remains low, even during forecasts of opportunity. A spring skill minimum is also evident in theoretical expected skill, indicating a reduced signal-to-noise ratio during spring that obscures predictable anomaly growth and renders subseasonal spring forecasts generally less skillful than those initialized during winter and summer.

Our results are consistent with the minimum in weeks 3-4 2mT skill found over CONUS in March – May (MAM) in the NCEP model by Wang and Robertson (2018). The same study showed the IFS showed a minimum in skill during MAM as well, but only over portions of North America, most notably the central and eastern United States. However, we note that since March includes at least a portion of the winter phase of the jet during most years (Fig. 1), a comparison to MAM skill and the spring skill evaluated in this study may not be the most direct. The spring minimum found in this study is also consistent with the skill reduction in the IFS subseasonal north Pacific jet forecasts during April and May, compared to March, that is shown by Albers et al. (2021), suggesting the spring minimum in skill is not limited to the LIM framework, but likely reflects a true limitation to subseasonal predictability in the PNA region.

The OPs that develop during spring are associated with a propagating heating anomaly, potentially suggesting the MJO is important for spring forecasts of opportunity. Conversely, predictable winter and summer 2mT patterns are associated with stationary and persistent tropical convective heating anomalies, though they differ in heating location and the associated circulation and 2mT structures. Such a heating source could be a key element to their enhanced subseasonal 2mT skill, particularly during forecasts of opportunity (Mayer and Barnes 2021).

Furthermore, the wintertime stratospheric polar vortex could contribute to the elevated winter signal observed in Figure 7, given its known influence on the circulation (Albers and Newman 2021a) and surface temperature (Butler et al. 2019a,b; Domeisen et al. 2020). To dynamically isolate these remote influences from tropical heating and the stratosphere, future work could employ the decoupling approach of Albers and Newman (2021) to reexamine subseasonal 2mT forecast skill and forecasts of opportunity.

Despite the presence of stationary tropical heating in both phases, the OPs that develop in winter and summer differ markedly, including their spatial structure, with winter OPs producing larger-scale waves than summer OPs. Still, both are associated with periods of elevated forecast skill, suggesting smaller-scale patterns aren't necessarily less predictable than large-scale patterns. Summer also benefits from the lowest noise amplitude of the three phases, so while the overall amplitude of the signal in summer is far weaker than in winter, the patterns are still predictable, as supported by the success of the forecasts of opportunity in summer (Figs. 5-6).

Changes in remote SST and stratospheric forcing are not the only potential underlying reasons for the spring minimum in skill. For example, Breeden et al. (2021) found an invigorated storm track during spring, which could mean that synoptic variability – approximated with the noise forcing term in Eqn 2 – is too high to realize the signal associated with OP1 or OP2, as suggested in Figure 7. Alternatively, variables crucial for spring prediction could be missing from the state vector, although to have a big impact on model performance they would have to contain relevant information that is not implicitly captured in the original variables. Still, we note that the LIMs developed here are relatively simple, and the influence of additional variables can be easily tested. Finally, the LIMs are constructed using the fluctuation-dissipation relationship, assuming that the covariance of the system is constant with time (Penland and Sardeshmukh 1995). It is possible that, even defining spring on a flow-dependent basis as done in this study, that the mean state and variance are changing too rapidly during the transition season to be modeled effectively by the LIM under this assumption. Future work will consider how forecast skill compares between dynamical subseasonal models and LIMs, to better discern which of these factors most strongly impacts subseasonal skill.

Acknowledgements

This research was supported by the NOAA Climate and Global Change Postdoctoral Fellowship Program, administered by UCAR's Cooperative Programs for the Advancement of Earth System Science (CPAESS) under award # NA18NWS4620043B.

Data Availability

The reanalysis data used for this project, JRA-55 (Kobayashi et al. 2015), is freely available from the National Center for Atmospheric Research / University Consortium for Atmospheric Research (NCAR / UCAR) Research Data Archive:

<https://rda.ucar.edu/datasets/ds628.8/index.html#!access>.

REFERENCES

- Albers, J. R. and Newman, M., 2019: A priori identification of skillful extratropical subseasonal forecasts, *Geophys. Res. Lett.*, 46, 12527–12536, <https://doi.org/10.1029/2019GL085270>.
- Albers, J. R. and M. Newman, 2021a: Subseasonal predictability of the North Atlantic Oscillation, *Environmental Research Letters*, **16** (4), 044024.
- Albers, J. R., Butler, A. H., Breeden, M. L., Langford, A. O., and G. N. Kiladis, 2021b: Subseasonal prediction of springtime Pacific–North American transport using upper-level wind forecasts, *Weather Clim. Dynam.*, 2, 433–452, <https://doi.org/10.5194/wcd-2-433-2021>.
- Baldwin M P, Stephenson D B, Thompson D W, Dunkerton T J, Charlton A J and O'Neill A 2003 Stratospheric memory and skill of extended-range weather forecasts, *Science*, **301**, 636–40.
- Betancourt, J., M. Schwartz, D. Breshears, D. Cayan, M. Dettinger, D. Inouye, E. Post, and B. Reed, 2005: Implementing a U.S. National Phenology Network. *Eos, Trans. Amer. Geophys. Union*, 86, 51, doi:10.1029/2005EO510005.
- Boyd, J. P., 1983: The continuous spectrum of linear Couette flow with the beta effect. *J. Atmos. Sci.*, **40**, 2304–2308.

499

500 Breeden, M. L. and J. E. Martin, 2018: Analysis of the onset of an extreme North Pacific Jet
 501 Retraction using Piecewise Tendency Diagnosis, *Quart. J. Roy. Meteor. Soc.*, **144**, 1895-1913.
 502 doi: 10.1002/qj.3388.

503

504 Breeden, M. L., B. T. Hoover, M. Newman, and D. J. Vimont, 2020: Optimal North Pacific
 505 Blocking Precursors and Their Deterministic Subseasonal Evolution during Boreal Winter. *Mon.*
 506 *Wea. Rev.*, **148**, 739–761, <https://doi.org/10.1175/MWR-D-19-0273.1>.

507

508 Breeden, M. L., Butler, A. H., Albers, J. R., Sprenger, M., and A. O. Langford, 2021: The spring
 509 transition of the North Pacific jet and its relation to deep stratosphere-to-troposphere mass
 510 transport over western North America, *Atmos. Chem. Phys.*, **21**, 2781–2794,
 511 <https://doi.org/10.5194/acp-21-2781-2021>.

512

513 Butler, A., Charlton-Perez, A., Domeisen, D.I. V, Garfinkel, C., Gerber, E.P., Hitchcock, P.,
 514 Karpechko, A.Y., Maycock, A.C., Sigmond, M., Simpson, I. & Son, S.-W., 2019a: Chapter 11 -
 515 Sub-seasonal Predictability and the Stratosphere. In A. W. Robertson & F. Vitart, eds. *Sub-*
 516 *Seasonal to Seasonal Prediction*. Elsevier, pp. 223–241. doi: [https://doi.org/10.1016/B978-0-12-](https://doi.org/10.1016/B978-0-12-811714-9.00011-5)
 517 [811714-9.00011-5](https://doi.org/10.1016/B978-0-12-811714-9.00011-5).

518

519 Butler, A. H., Charlton-Perez, A., Domeisen, D. I. V., Simpson, I., & J. Sjoberg,
 520 2019b: Predictability of Northern Hemisphere final stratospheric warmings and their surface
 521 impacts. *Geophysical Research*
 522 *Letters*, **46**, 10,578– 10,588, <https://doi.org/10.1029/2019GL083346>.

523

524 Cash, B. A., and S. Lee, 2001: Observed nonmodal growth of the Pacific-North American
 525 teleconnection pattern. *J. Clim.*, **14**, 1017–1028, <https://doi.org/10.1175/1520-0442>.

526

527 de Andrade, F. M., C. A. S. Coelho, and I. F. A. Cavalcanti, 2019: Global precipitation hindcast
 528 quality assessment of the Subseasonal to Seasonal (S2S) prediction project models. *Climate*
 529 *Dyn.*, **52**, 5451–5475, <https://doi.org/10.1007/s00382-018-4457-z>.

530

531 Domeisen, D. I., Butler, A. H., Charlton-Perez, A. J., Ayarzagüena, B., Baldwin, M. P., Dunn-
 532 Sigouin, E. et al., 2020: The role of the stratosphere in subseasonal to seasonal prediction:2.
 533 Predictability arising from stratosphere-troposphere coupling. *Journal of Geophysical Research:*
 534 *Atmospheres*, 125, e2019JD030923. <https://doi.org/10.1029/2019JD030923>.
 535

536 Farrell, B. F., 1982: The initial growth of disturbances in a baroclinic flow. *J. Atmos. Sci.*, **39**,
 537 1663–1686, <https://doi.org/10.1175/1520-0469>.
 538

539 Farrell, B. F., 1988: Optimal excitation of neutral Rossby waves. *J. Atmos. Sci.*, **45**, 163–172,
 540 <https://doi.org/10.1175/1520-0469>.
 541

542 Farrell, B. F., and P. J. Ioannou, 1996: Generalized Stability Theory. Part I: Autonomous
 543 Operators. *J. Atmos. Sci.*, **52**, 2025–2040, [https://doi.org/10.1175/1520-](https://doi.org/10.1175/1520-0469(1996)053<2025:GSTPIA>2.0.CO;2)
 544 [0469\(1996\)053<2025:GSTPIA>2.0.CO;2](https://doi.org/10.1175/1520-0469(1996)053<2025:GSTPIA>2.0.CO;2).
 545

546 Gerber, E. P., Butler, A., Calvo, N., Charlton-Perez, A., Giorgetta, M., Manzini, E., Perlwitz, J.,
 547 Polvani, L. M., Sassi, F., Scaife, A. A., Shaw, T. A., Son, S., & S. Watanabe, 2012: Assessing
 548 and Understanding the Impact of Stratospheric Dynamics and Variability on the Earth
 549 System, *Bulletin of the American Meteorological Society*, **93(6)**, 845-859.
 550

551 Henderson S. A., Vimont D. J. and M. Newman, 2020: The critical role of non-normality in
 552 partitioning tropical and extratropical contributions to PNA growth, *J. Clim.*, **33**, 6273–95,
 553 <https://doi.org/10.1175/JCLI-D-19-0555.1>.

554 Johnson, N. C., Collins, D. C., Feldstein, S. B., L’Heureux, M. L., and E. E. Riddle, 2014:
 555 Skillful wintertime north American temperature forecasts out to 4 weeks based on the state of
 556 ENSO and the MJO. *Weather Forecast.* 29, 23–38. doi: 10.1175/WAF-D-13-00102.1

557 Jong, B.-T., M. Newman, and A. Hoell, 2022: Subseasonal Meteorological Drought
 558 Development over the Central United States during Spring. *J. Climate*, doi: 10.1175/JCLI-D-21-
 559 0435.1.

560

561 Kobayashi, S., Ota, Y., Harada, Y., Ebita, A., Moriya, M., Onoda, H., Onogi, Kamahori, H.,
 562 Kobayashi, C., Hirokazu, E., Miyaoka, K., and K. Takahashi, 2015: The JRA- 55 reanalysis:
 563 General specifications and basic characteristics. *Journal of the Meteorological Society of Japan*.
 564 *Ser. II*, 93(1), 5–48. <https://doi.org/10.2151/jmsj.2015-001>.
 565

566 Koster, R. D., Mahanama, S. P. P., Yamada, T. J., Balsamo, G., Berg, A. A., Boisserie, M.,
 567 Dirmeyer, P. A., Doblas-Reyes, F. J., Drewitt, G., Gordon, C. T., Guo, Z., Jeong, J., Lee, W., Li,
 568 Z., Luo, L., Malyshev, S., Merryfield, W. J., Seneviratne, S. I., Stanelle, T., van den Hurk, B. J.
 569 J. M., Vitart, F., & Wood, E. F. (2011). The Second Phase of the Global Land–Atmosphere
 570 Coupling Experiment: Soil Moisture Contributions to Subseasonal Forecast Skill, *Journal of*
 571 *Hydrometeorology*, 12(5), 805-822.
 572

573 Lacarra, J.-F., and O. Talagrand, 1988: Short range evolution of small perturbations in a
 574 barotropic model. *Tellus*, **40A**, 81–95.
 575

576 Madden, R. A., and P. R. Julian, 1971: Detection of a 40–50 Day Oscillation in the Zonal Wind
 577 in the Tropical Pacific, *Journal of Atmospheric Sciences*, 28(5), 702-708.
 578

579 Mak, M. and M. Cai, 1989: Local barotropic instability. *Journal of the Atmospheric Sciences*, **46**,
 580 3289–3311.
 581

582 Mariotti, A., Baggett, C., Barnes, E. A., Becker, E., Butler, A., Collins, D. C., Dirmeyer, P. A.,
 583 Ferranti, L., Johnson, N. C., Jones, J., Kirtman, B. P., Lang, A. L., Molod, A., Newman, M.,
 584 Robertson, A. W., Schubert, S., Waliser, D. E., & Albers, J. (2020). Windows of Opportunity for
 585 Skillful Forecasts Subseasonal to Seasonal and Beyond, *BAMS*, 101(5), E608-E625.
 586

587 Mayer, K. J., and E. A. Barnes, 2021: Subseasonal forecasts of opportunity identified by an
 588 explainable neural network. *Geophysical Research Letters*, **48**, e2020GL092092. [https://doi.](https://doi.org/10.1029/2020GL092092)
 589 [org/10.1029/2020GL092092](https://doi.org/10.1029/2020GL092092).
 590

Newman, M., and P. D. Sardeshmukh, 1998: The impact of the annual cycle on the North Pacific/North American response to remote low-frequency forcing. *J. Atmos. Sci.*, **55**, 1336–1353.

Newman, M., Sardeshmukh, P. D., Winkler, C. R., and J. S. Whitaker, 2003: A study of subseasonal predictability. *Monthly Weather Review*, **131**(8), 1715–1732.
<https://doi.org/10.1175//2558.1>.

Pegion, K., Kirtman, B. P., Becker, E., Collins, D. C., LaJoie, E., Burgman, R., Bell, R., DelSole, T., Min, D., Zhu, Y., Li, W., Sinsky, E., Guan, H., Gottschalck, J., Metzger, E. J., Barton, N. P., Achuthavarier, D., Marshak, J., Koster, R. D., Lin, H., Gagnon, N., Bell, M., Tippett, M. K., Robertson, A. W., Sun, S., Benjamin, S. G., Green, B. W., Bleck, R., and H. Kim, 2019: : The Subseasonal Experiment (SubX): A multi-model subseasonal prediction experiment. *Bull. Amer. Meteor. Soc.*, <https://doi.org/10.1175/BAMS-D-18-0270.1>.

Penland, C. and P. D. Sardeshmukh, 1995: The optimal growth of tropical sea surface temperature anomalies *J. Clim.* **8**, 1999–2024.

Sardeshkmukh, P., M. Newman, and M. D. Borges, 1997: Free barotropic Rossby wave dynamics of the wintertime low-frequency flow. *J. Atmos. Sci.*, **54**, 5–23.

Sardeshmukh, P. D., Compo, G. P., and C. Penland, 2000: Changes of Probability Associated with El Niño, *Journal of Climate*, **13**(24), 4268-4286.

Vigaud, N., Robertson, A. W., and M. K. Tippett, 2018: Predictability of recurrent weather regimes over North America during winter from submonthly reforecasts. *Monthly Weather Review*, **146**(8), 2559–2577. <https://doi.org/10.1175/MWR-D-18-0058.1>.

Wang, L., and A. W. Robertson, 2018: Week 3-4 Predictability over the United States assessed from two operational ensemble prediction systems, *Clim. Dyn.*, 52:5861–5875
<https://doi.org/10.1007/s00382-018-4484-9>.

621 Winkler, C. R., M. Newman, and P. D. Sardeshmukh, 2001: A linear model of wintertime low-
622 frequency variability. Part I: Formulation and forecast skill. *J. Climate*, **14**, 4474–4494.